Simulated non-thermal emission of the supernova remnant G1.9+0.3

M. A. Villagran[1], D. O. Gómez[1], P. F. Velázquez[2], D. M.-A. Meyer[3], A. Chiotellis[4], A. C. Raga[2], A. Esquivel[2], J. C. Toledo-Roy[2], K. M. Vargas-Rojas[2] & E.M. Schneiter[5]

[1]Instituto de Astronomía y Física del Espacio, Argentina; [2]Instituto de Ciencias Nucleares, UNAM, Mexico; [3]Institut für Physik und Astronomie, U Postdam, Germany; [4]Institute for Astronomy, Astrophysics, Space Applications and Remote Sensing, National Observatory of Athens, Greece, [5]Departamento de Materiales y Tecnología, FCEFyN-UNC, Argentina.

Abstract

Supernova remnants are the nebular leftover of defunct stellar environments, resulting from the interaction between a supernova blast wave and the circumstellar medium shaped by the progenitor throughout its life. They display a large variety of non-spherical morphologies such as ears that shine non-thermally. We have modeled the structure and the non-thermal emission of the supernova remnant G1.9+0.3 through 3D magnetohydrodynamic numerical simulations. We propose that the peculiar ear-shaped morphology of this supernova remnant results from the interaction of its blast wave with a magnetized circumstellar medium, which was previously asymmetrically shaped by the past stellar wind emanating from the progenitor star or its stellar companion. We created synthetic non-thermal radio and X-ray maps from our simulated remnant structure, which are in qualitative agreement with observations, forming ears on the polar directions. Our synthetic map study explains the discrepancies between the measured non-thermal radio and X-ray surface brightness distributions assuming that the inverse Compton process produces the observed X-ray emission.

1 Introduction

Supernova remnant (SNR) G1.9+0.3 is the youngest galactic remnant (Reynolds et al. 2008), ranging in age from 100 to 150 yr and probably resulting from a type Ia explosion (Borkowski et al. 2017). It exhibits an incomplete shell morphology in the radio continuum (see Fig. 1a) with an enhancement towards the north (spectral index of -0.6; Luken et al. 2020). In X-rays, the remnant appears elongated with two bright arcs to the south-east and north-west (Reynolds et al. 2008; see Fig. 1b). This striking difference between the radio and X-ray appearances is one of the most intriguing features of this remnant. While the X-ray emission can be due to the synchrotron process, it is difficult to conceive how it could result in such different morphology, if the mechanism is the same as in radio. Numerical models of the remnant have explored expansion into inhomogenous ambient mediums (Borkowski et al. 2017) or from within a planetary nebula (Tsebrenko & Soker 2015), with mixed results. In this work, we propose that the X-ray emission comes from the inverse Compton (IC) mechanism, allowing for geometries not directly coupled to the magnetic field.

Figure 1. (a) VLA image at 1365 MHz. (b) Chandra image at 1.2-8 keV (colors) with overlaid radio contours.

2 MHD Simulations

2.1 The Scenario

Our goal is to model the complex non-thermal emission morphology of the remnant through MHD simulations. A key idea in explaining highly asymmetric morphologies is expansion of the supernova (SN) blast wave into an asymmetric circumstellar medium produced by the progenitor or companion stellar wind (e.g. Blondin et al. 1996, Chiotellis et al. 2020, 2021, Velázquez et al. 2023).
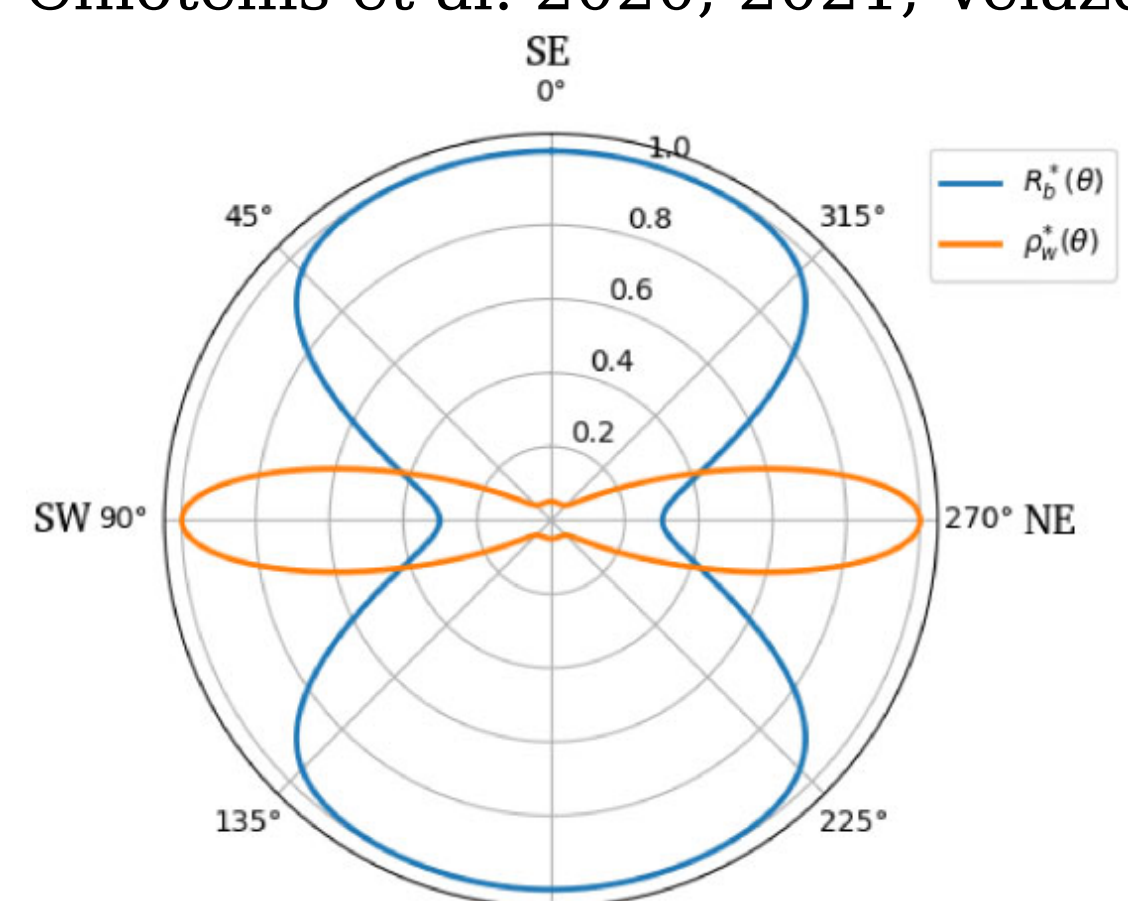
Figure 2. Density and radius polar profiles of the asymmetric pre-SN wind.

For the asymmetric pre-SN stellar wind we follow the prescription of Mellema, Eudelrink & Icke (1991), where the wind density and velocity depend on the radius r and polar angle θ as:

$$\rho_w(\theta, r) = \frac{\dot{M}_w}{4\pi v_p r^2} f(\theta) \qquad v_w(\theta) = \frac{v_p}{f(\theta)}$$

where $\dot{M}_w$ is the mass-loss rate and v_p the terminal velocity of the wind at the pole, and the function $f(\theta;\alpha,\beta)$ determines the equator-to-pole density ratio and the width of the equatorial region (see the paper for more details). We chose α=0.95 and β=5, resulting in the wind density (orange line) and bubble radius (blue) profiles shown in Fig. 2.

In model R1, the pre-SN wind expands into an homogeneous ambient medium with n_0=0.25 cm^{-3}, T=1000 K and B_0=1μG. Following Zhang et al. (2023), we also explored (model R2) the possibility of a medium with an exponential density towards the north-east. In both models, after evolving the wind for 150 kyr, a type Ia SN explosion with E_0=10^{51} erg and M_{ej}=1.38 M$_\odot$ is imposed and numerically integrated for 140 yr.

2.2 The Code

We use the parallel 3D magnetohydrodynamical code GUACHO (Esquivel et al. 2009; Villareal D'Angelo et al. 2018), which solves the ideal MHD equations in a fixed 3D Cartesian grid using a second-order Godunov method with the HLLD approximate Riemann solver (Miyoshi & Kusano 2005). The code includes radiative cooling following Dalgarno & McCray (1972). Outflow conditions are imposed on all domain boundaries.

2.3 Synthetic emission maps

In order to compare with the observed morphologies, from the results of the numerical simulations we compute radio synchrotron and X-ray synthetic emission maps.

2.3.1 Radio synchrotron emission

Synchrotron emission is produced when particles accelerated to relativistic energies by the SN shock wave encounter magnetic fields, which can also be strengthened by shock compression of the plasma. To estimate this radio emission, in each computational cell we impose a distribution of relativistic electron density and energies, use it to estimate the synchrotron emissivity following the methodology of Ghisellini (2013), and finally integrate the emission along the line of sight to create a 2D map; see paper for details.

$$N_e(\gamma) = K\gamma^{-p} \qquad \chi_n n_g = n_e = \int_{\gamma_{min}}^{\infty} K\gamma^{-p} d\gamma \simeq \frac{K}{p-1}\gamma_{min}^{-p+1}$$

$$j_s(\nu,\theta) = \frac{3\sigma_T c K U_B}{8\pi^2 \nu_L}(\sin\theta)^{(p+1)/2}\left(\frac{\nu}{\nu_L}\right)^{-(p-1)/2} f_s(p) \qquad I(x',y',\nu) = \int_{LoS} j_s(x',y',z',\nu)dz'$$

2.3.2 Inverse Compton X-ray emission

A possible source for the non-thermal X-ray emission, different from synchrotron, is the Inverse Compton (IC) process, wherein low-energy photons are boosted to high energies by their interaction with relativistic electrons. We use the prescription of Ghisellini (2013) to compute the IC emissivity from two possible photon sources (ambient Hα emission and the parameterized radiative cooling of the plasma) and compute emission maps as described above.

$$\epsilon(\nu_c) = \frac{1}{4\pi}\frac{(4/3)^\alpha}{2}\sigma_T c K \frac{U_r}{\nu_0}\left(\frac{\nu_c}{\nu_0}\right)^{-\alpha} \qquad U_r = \frac{3}{4}\frac{R}{c}4\pi\epsilon_{H\alpha}(\nu_{H\alpha}) \qquad U_r = \frac{3}{4}\frac{R}{c}Q_L$$

3 Results

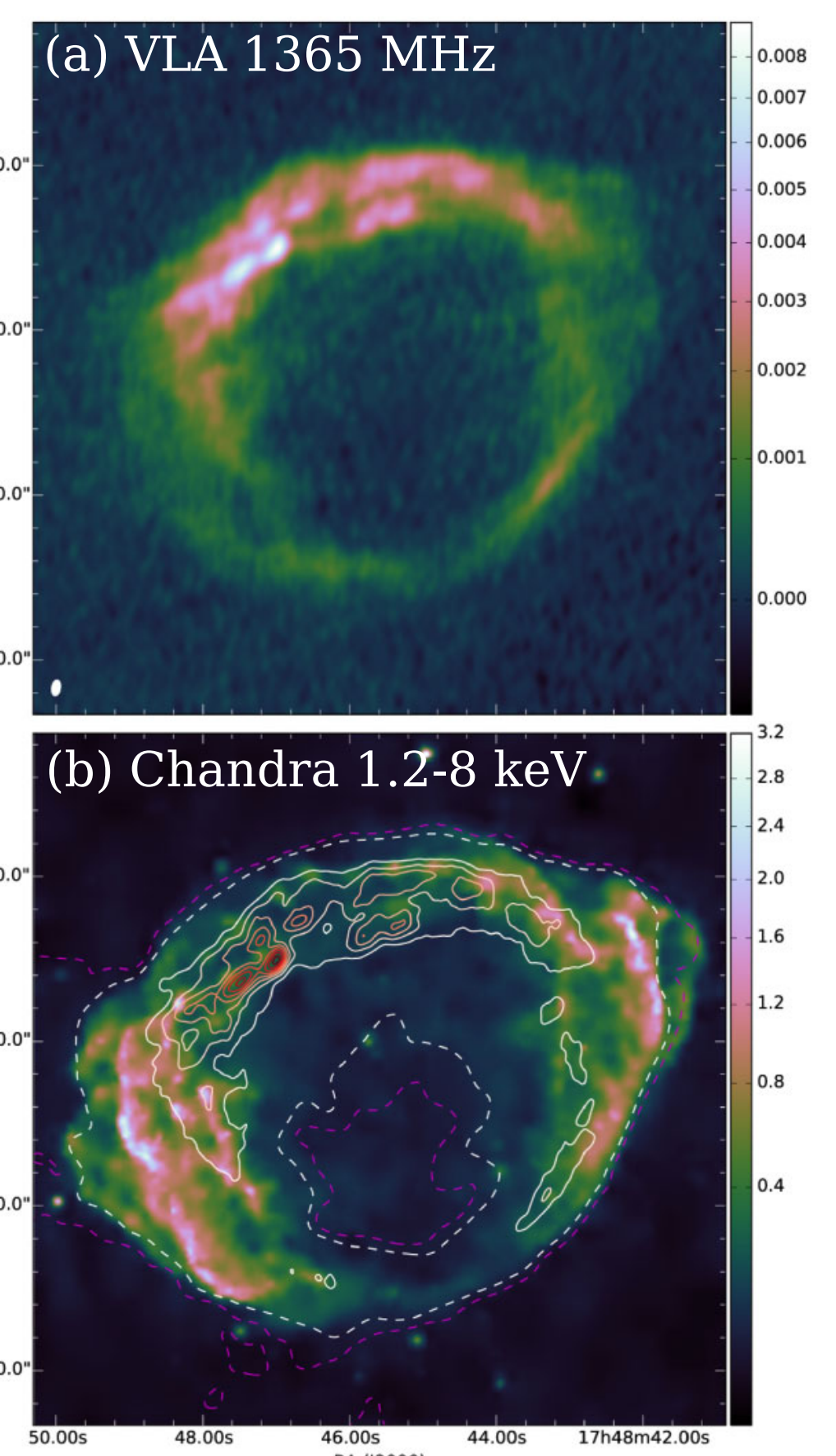### 3.1 Physical structure

The 3D MHD simulations resulted in two key moments for each of the models R1 and R2: the first one at 150 kyr, after the pre-SN stellar wind has plowed a bipolar bubble around the progenitor system. At that moment, the SN explosion is imposed and left to evolve inside this structure. The second key moment is 140 yr after the explosion, where the SNR has grown to ~2 pc in size. The resulting slices of the density (top row, blue), temperature (middle row, red) and magnetic field intensity (bottom row, green) at each of these two key moments, for models R1 (left columns) and R2 (right columns) are shown in Figure 3.
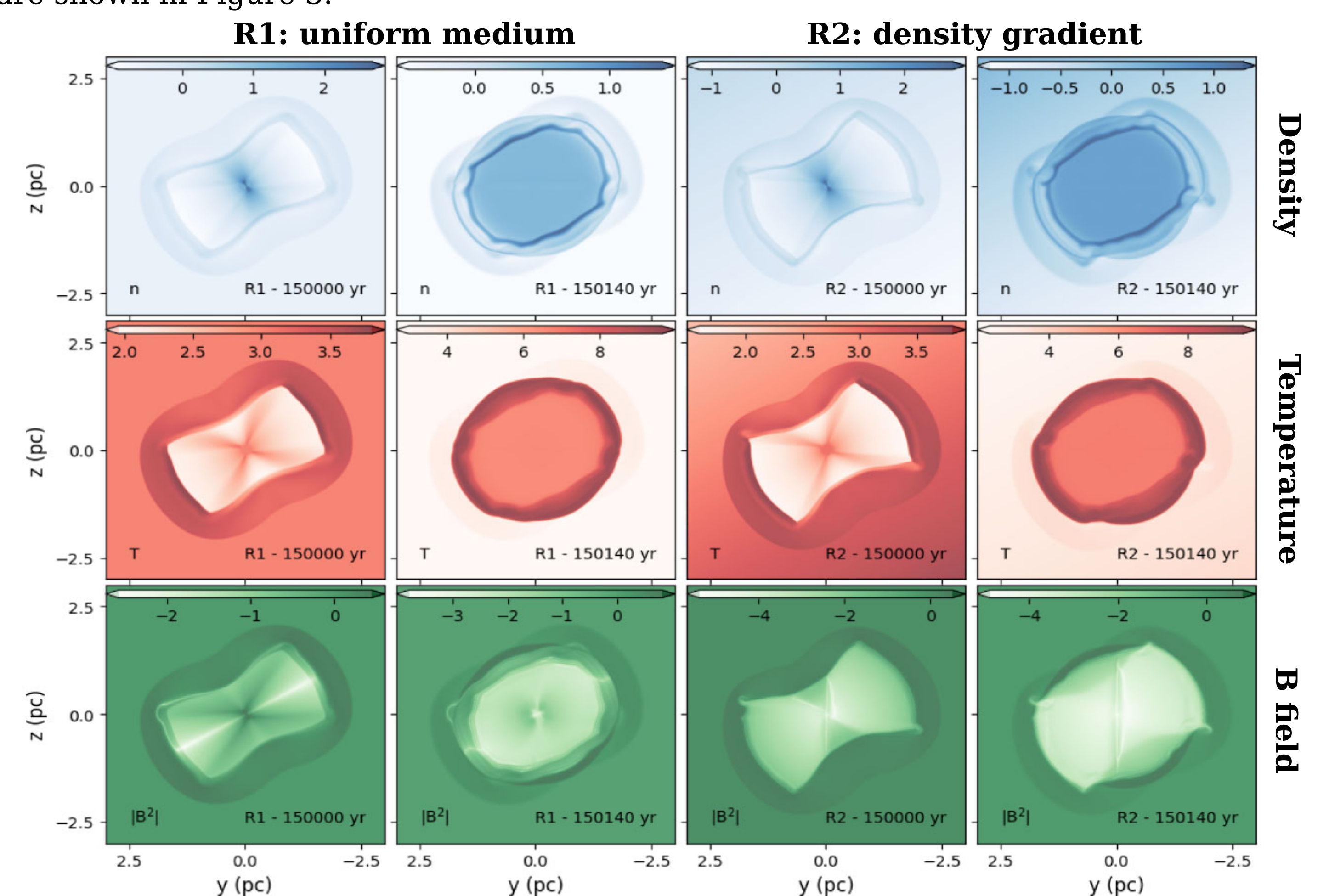
Figure 3. Density, temperature and magnetic field intensity slices of the MHD simulations after the pre-SN wind phase and after the 140 yr evolution of the SN explosion.

3.2 Synthetic emission maps

The computed maps for the 2.1 GHz synchrotron radio and 2-10 keV inverse Compton X-ray emissions are shown in Fig. 4 and Fig. 5, respectively, for both models, after SNR expansion. We see that the radio maps (Fig. 4) show enhancements along the NE-SW line, with a stronger NE arc –more consistent with the observations– in the R2 model. Meanwhile, the IC X-ray emission exhibits a more complete ring-like structure with enhancements along the SW-NE line, perpendicular to that of the radio maps; model R2 again shows a slight enhancement to the NE (towards the density gradient).
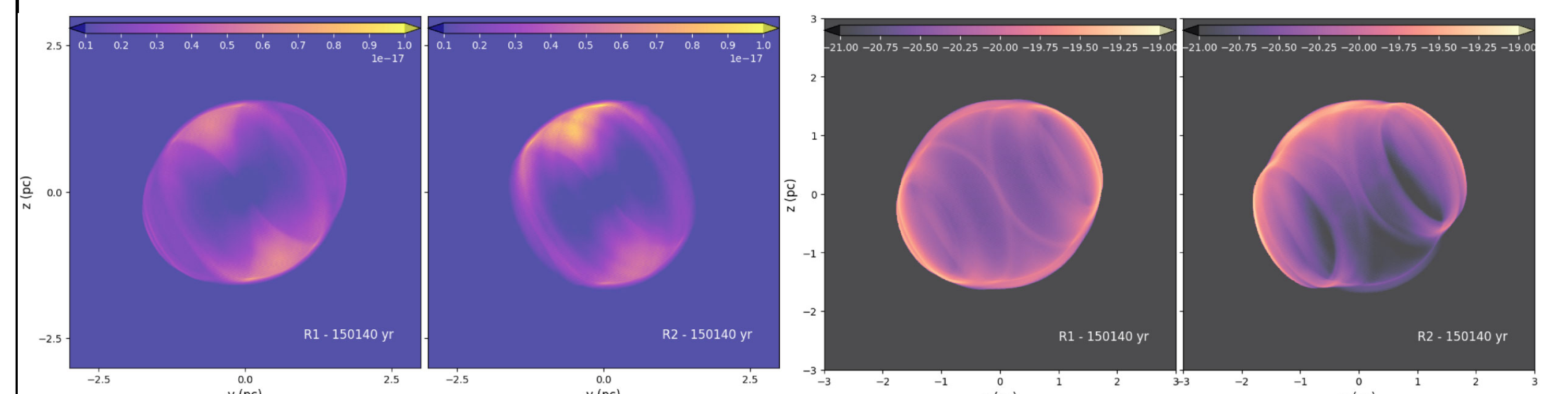
Figure 4. Radio synchrotron emission maps at 2.1Ghz for both models.

Figure 5. X-ray inverse Compton emission maps for a 2-10 keV band for both models.

4 Conclusions

• The peculiar, mixed morphology of G1.0+0.3 can be explained by an SNR expanding into the bipolar bubble plowed by the asymmetric stellar wind from the progenitor.

• The pronounced discrepancy between the radio synchrotron and X-ray emissions, both non-thermal, is reconciled by a different origin for the X-rays: inverse Compton.

• A gradient in the ambient density around the object can explain the observed enhancement of the emission on the NE side (more pronounced for radio).

References

Blondin J. M., Lundqvist P., Chevalier R. A., 1996, ApJ, 472, 257
Borkowski K. J., Gwynne P., Reynolds S. P., Green D. A., Hwang U., Petre R., Willett R., 2017, ApJ, 837, L7
Chiotellis A., Boumis P., Spetsieri Z. T., 2020, Galaxies, 8, 38
Chiotellis A., Boumis P., Spetsieri Z. T., 2021, MNRAS , 502, 176
Dalgarno A., McCray R. A., 1972, ARA&A, 10, 375
Ghisellini G., 2013, Radiative Processes in High Energy Astrophysics. Springer International Publishing, Switzerlandhttps:// doi.org/10.1007%2F978-3-319-00612-3
Luken K. J. et al., 2020, MNRAS, 492, 2606
Miyoshi T., Kusano K., 2005, J. Comput. Phys., 208, 315
Reynolds S. P., Borkowski K. J., Green D. A., Hwang U., Harrus I., Petre R., 2008, ApJ, 680, L41
Tsebrenko D., Soker N., 2015, MNRAS, 450, 1399
Velázquez P . F., Meyer D. M. A., Chiotellis A., Cruz-Álvarez A. E., Schneiter E. M., Toledo-Roy J. C., Reynoso E. M., Esquivel A., 2023, MNRAS, 519, 5358
Zhang S., Tian W., Zhang M., Zhu H., Cui X., 2023, ApJ, 942, 94